Title: Recent climate variability in Antarctica from satellite-derived temperature data

Authors: David P. Schneider[1], Eric J. Steig[1], and Josefino C. Comiso[2]

[1]Department of Earth and Space Sciences, University of Washington, Box 351310

Seattle, WA 98195, email: schneidd@u.washington.edu

[2]Ocean and Ice Branch, Code 971, NASA Goddard Space Flight Center

Greenbelt, MD 20771 email: comiso@joey.gsfc.nasa.gov

Abstract

Recent Antarctic climate variability on month-to-month to interannual time scales is assessed through joint analysis of surface temperatures from satellite thermal infrared observations (T_{IR}) and passive microwave brightness temperatures (T_B). Although T_{IR} data are limited to clear-sky conditions and T_B data are a product of the temperature and emissivity of the upper $\sim$ 1m of snow, the two data sets share significant covariance. This covariance is largely explained by three empirical modes, which illustrate the spatial and temporal variability of Antarctic surface temperatures. T_B variations are damped compared to T_{IR} variations, as determined by the period of the temperature forcing and the microwave emission depth; however, microwave emissivity does not vary significantly in time. Comparison of the temperature modes with Southern Hemisphere (SH) 500-hPa geopotential height anomalies demonstrates that Antarctic temperature anomalies are predominantly controlled by the principal patterns of SH atmospheric circulation. The leading surface temperature mode strongly correlates with the Southern Annular Mode (SAM) in geopotential height. The second temperature mode reflects the combined influences of the zonal wavenumber-3 and Pacific South American (PSA) patterns in 500-hPa height on month-to-month timescales. ENSO variability projects onto this mode on interannual timescales, but is not by itself a good predictor of Antarctic temperature anomalies. The third temperature mode explains winter warming trends, which may be caused by blocking events, over a large region of the East Antarctic plateau. These results help to place recent climate changes in the context of Antarctica's background climate variability and will aid in the interpretation of ice core paleoclimate records.

Popular Science Summary

The Antarctic region is known to be an anomalous region since cooling is observed in the eastern high latitude regions while the western region show predominant warming, especially in the Antarctic Peninsula. The variability of the climate in the region is studied on month-to-month to interannual time scales through joint analysis of surface temperatures from satellite thermal infraredobservations (T_{IR}) and passive microwave brightness temperatures (T_B). Although T_{IR} data are limited to clear-sky conditions and T_B data are a product of the temperature and emissivity of the upper ~ 1m of snow, the two data sets share significant covariance. This covariance is largely explained by three empirical modes, which illustrate the spatial and temporal variability of Antarctic surface temperatures. T_B variations are damped compared to T_{IR} variations, as determined by the period of the temperature forcing and the microwave emission depth; however, microwave emissivity does not vary significantly in time. Comparison of the temperature modes with Southern Hemisphere (SH) 500-hPa geopotential height anomalies demonstrates that Antarctic temperature anomalies are predominantly controlled by the principal patterns of SH atmospheric circulation. The leading surface temperature mode strongly correlates with the Southern Annular Mode (SAM) in geopotential height. The second temperature mode reflects the combined influences of the zonal wavenumber-3 and Pacific South American (PSA) patterns in 500-hPa height on month-to-month timescales. ENSO variability projects onto this mode on interannual timescales, but is not by itself a good predictor of Antarctic temperature anomalies. The third temperature mode explains winter warming trends, which may be caused by blocking events, over a large region of the East Antarctic plateau. These results help to place recent climate changes in the context of Antarctica's background climate variability and will aid in the interpretation of ice core paleoclimate records.

Recent climate variability in Antarctica from satellite-derived temperature data

David P. Schneider and Eric J. Steig*

Department of Earth and Space Sciences, University of Washington, Seattle, Washington

Josefino C. Comiso

Laboratory for Hydrospheric Processes, NASA Goddard Space Flight Center, Greenbelt, Maryland

*Also at *Quaternary Research Center, University of Washington, Seattle Washington*

Corresponding author address:
David Schneider
Department of Earth and Space Sciences
University of Washington
Box 351310
Seattle, WA 98195
tel: 206-543-6223, 206-543-6327
FAX: 206-543-0489
email: schneidd@u.washington.edu

[TECHNICAL NOTE: All Figures will be made available as separate high quality .EPS files when necessary for publication]

ABSTRACT

Recent Antarctic climate variability on month-to-month to interannual time scales is assessed through joint analysis of surface temperatures from satellite thermal infrared observations (T_{IR}) and passive microwave brightness temperatures (T_B). Although T_{IR} data are limited to clear-sky conditions and T_B data are a product of the temperature and emissivity of the upper $\sim 1m$ of snow, the two data sets share significant covariance. This covariance is largely explained by three empirical modes, which illustrate the spatial and temporal variability of Antarctic surface temperatures. T_B variations are damped compared to T_{IR} variations, as determined by the period of the temperature forcing and the microwave emission depth; however, microwave emissivity does not vary significantly in time. Comparison of the temperature modes with Southern Hemisphere (SH) 500-hPa geopotential height anomalies demonstrates that Antarctic temperature anomalies are predominantly controlled by the principal patterns of SH atmospheric circulation. The leading surface temperature mode strongly correlates with the Southern Annular Mode (SAM) in geopotential height. The second temperature mode reflects the combined influences of the zonal wavenumber-3 and Pacific South American (PSA) patterns in 500-hPa height on month-to-month timescales. ENSO variability projects onto this mode on interannual timescales, but is not by itself a good predictor of Antarctic temperature anomalies. The third temperature mode explains winter warming trends, which may be caused by blocking events, over a large region of the East Antarctic plateau. These results help to place recent climate changes in the context of Antarctica's background climate variability and will aid in the interpretation of ice core paleoclimate records.

1. Introduction

A number of studies have shown considerable interest in identifying and explaining Antarctic temperature trends over recent decades (Doran et al. 2002; Marshall 2002a; Thompson and Solomon 2002; Vaughan et al. 2001; van den Broeke 2000a). However, because the interannual variability of Antarctic climate is large, it is difficult to establish the significance of surface temperature trends from sparsely distributed weather stations on the continent (King 1994). Furthermore, relatively little is known about the spatial structure of surface temperature variations across Antarctica. Such knowledge would, for example, improve the interpretation of ice core paleoclimate records, which are usually obtained from locations that are remote from weather stations.

Two important influences on Antarctica's climate variability, the Southern Annular Mode (SAM) and the El Niño-Southern Oscillation (ENSO), have been discussed by several studies, and increased tendency for these circulation patterns to stay in a particular phase may be driving surface temperature trends in the Antarctic (Gillett and Thompson 2003; Bromwich et al. 2003; Ribera and Mann 2003; Thompson and Solomon 2002; Kwok and Comiso 2002). We are therefore motivated to pay particular attention to the influence of these atmospheric patterns on Antarctic surface temperature anomalies, which, in this study, are derived from passive microwave brightness temperature (T_B) and thermal infrared satellite observations (T_{IR}).

In previous work with these data, Schneider and Steig (2002; hereafter SS02) presented a principal component analysis of T_B data and showed evidence for the SAM and ENSO-related signals in Antarctica. However, the T_B data, taken alone, can be complicated to interpret because of the effects of non-stationary microwave emissivity variations due to variations in snow

characteristics, and occasional surface melt events. Kwok and Comiso (2002) examined newly available T_{IR} data, and also linked their variability to the SAM and ENSO. That study assumed, *a priori,* that indices of the SAM and ENSO would have skill in describing surface temperature anomalies, but it found mixed results. For example, the Southern Oscillation Index does explain SST and sea-ice anomalies well over the Southern Ocean, but it does not have good skill at describing temperature anomalies on the Antarctic continent. Also, as Comiso (2000) and Shuman and Comiso (2002) discuss, the T_{IR} data set is biased by the absence of data for days with cloud cover. Shuman and Comiso (2002) was the first study to directly compare T_{IR} and T_B data, and generally found good agreement, but it only made comparisons at a few isolated locations with weather stations. Given the sparse distribution of Antarctic weather stations, it is desirable to further examine Antarctic climate with these satellite data. Other gridded products, such as the NCEP-NCAR Reanalysis data, are significantly less reliable for Antarctic climate studies, especially for surface conditions (Marshall 2002b; Hines et al. 2000).

In this paper, we analyze the T_{IR} and T_B data in order to reduce uncertainties in interpreting either satellite data set alone. First, we evaluate the T_{IR} data with methods that optimize the amount of variance that can be explained, in parallel to SS02. Secondly, we use the two types of data to estimate the magnitude of microwave emissivity fluctuations. Finally, the data are evaluated jointly using Maximum Covariance Analysis (von Storch and Zweirs 1999). The results of this analysis increase confidence in the interpretation of both data sets in terms of surface temperature variability. We examine the relationship between surface temperature variability and atmospheric circulation through comparison of the empirical modes of the satellite data sets with NCEP-NCAR geopotential height data. We conclude that, overall, the SAM explains the greatest variance in Antarctic temperatures. However, the second most

important influence is not simply described by ENSO, but rather, reflects a combination of patterns previously referred to as the Pacific South American and wavenumber-3 patterns. We also suggest that blocking may be responsible for driving strong temperature trends in a little-studied region (0°-90°E) of East Antarctica.

2. Data

Surface temperature (T_{IR}) fields, at monthly resolution from January 1982 to December 1999, were derived for the Antarctic continent from thermal infrared channels of the Advanced Very High Resolution Radiometer (AVHRR) satellite as originally discussed by Comiso (2000). Comparison with available ground-based observations shows that T_{IR} data provide good estimates of the near-surface air temperature (T_a), although they may be cooler than the actual T_a under strong surface inversion conditions (Comiso 2000). In addition, monthly means of T_{IR} data have a clear-sky bias because infrared surface temperature estimates cannot be made in cloudy conditions. Since the net effect of clouds on surface temperature in the Antarctic is warming (e.g. King and Turner 1997), monthly cloud-free averages from the infrared observations tend to be cooler than *in situ* station observations by ~0.5 K (Comiso 2000). Originally constructed on a 6.25 x 6.25 km polar stereographic grid, the T_{IR} data are averaged to a 25 x 25 km grid, so that they are co-registered with the passive microwave data. Anomalies are computed by subtracting the monthly climatology at each grid point.

Passive microwave brightness temperature (T_B) data used in this study are from the 37 GHz vertically polarized channel on the Scanning Multichannel Microwave Radiometer (SMMR) and Special Sensor Microwave Imager (SSM/I) instruments on satellites from the same time period as the T_{IR} data. An important advantage of T_B data over T_{IR} data is that they can be obtained in all weather conditions. As discussed by SS02, T_B data cannot be interpreted as a

5

pure surface temperature signal, because the variability in microwave emissivity is not known. Attenuation of surface temperature changes through the penetration depth of the microwave emission—typically a few centimeters to a meter—means that amplitude is generally smaller for T_B variations than T_a variations. Surdyk (2002) emphasizes that changes in the snow temperature over the penetration depth have a much stronger influence on T_B variability than do emissivity changes. Surface melting, because of enhanced absorption of microwaves by liquid water during the melting event, and enhanced scattering after the snow re-freezes (Zwally and Fiegles 1994), accounts for the largest emissivity-forced component of T_B. This was evaluated by SS02, and found to be important primarily along the coast and on the ice shelves. A melt-masked, monthly anomaly dataset of T_B on the Antarctic continent is derived in the same manner as described by SS02 except where noted below.

Previous site-specific studies have found good agreement between T_{IR}, T_B, and T_a measurements made *in-situ* by Automatic Weather Stations (AWS). On monthly time scales, differences among the data have been found to be less than 1 K at most locations, if T_B data are corrected for emissivity (Shuman and Comiso 2002). However, these reported differences do not take into account the clear-sky bias, as AWS temperatures were compared to T_{IR} data only on days when both observations were available. Shuman and Comiso (2002) also found evidence for consistent offsets between T_a and T_{IR} data, notably a ~4 K difference across all temperatures at the South Pole. This offset, which may be due to covering the South Pole at scan angles off of nadir (Shuman and Comiso 2002), is not significant in our analysis because the mean T_{IR} values are subtracted from each grid point. Also, the T_B data are limited to areas north of 85°S, so the data sets are not directly compared in the South Pole region.

To examine the connections between the variability in Antarctic T_{IR} and T_B data and

larger-scale SH atmospheric circulation variability, 1982-1999 500-hPa geopotential height anomalies (Z500) poleward of 20°S, on a 2.5° x 2.5° latitude-longitude grid, are used from the NCEP-NCAR Reanalysis (NRA) (Kalnay et al. 1996; Kistler et al. 2001). Various biases, most importantly spurious multi-annual trends, have been reported in these data (Hines et al. 2000; Marshall 2002b) but should be of little consequence to the purposes of this study. The 500-hPa level is the lowest standard pressure surface entirely above the surface of the ice sheet and the stable inversion layer, and NRA 500-hPa data compare more favorably to Antarctic station observations than do 850-hPa geopotential height or surface pressure fields (Marshall 2002b, Hines et al. 2000).

3. Methods

In Section 4, principal component analysis (PCA) of T_{IR} anomaly data is performed. Empirical orthogonal function (EOF, spatial) patterns and principal components (PC, temporal variations) are computed for data from all months of the year and broken down by season, December-January-February (DJF), March-April-May (MAM), June-July-August (JJA), and September-October-November (SON). In Section 5, the data sets are compared qualitatively, and in Section 6, spatially and temporally varying microwave emissivity (ε) is estimated using the Rayleigh-Jeans approximation. Comparison of the T_{IR} and T_B fields through Maximum Covariance Analysis (MCA) is used in Section 7 to diagnose the common spatial-temporal signals in the two data sets. Heterogeneous regression maps are shown to illustrate the spatial patterns of the MCA modes, while expansion coefficients show temporal variations of the modes. Next, the leading T_{IR} and T_B expansion coefficients are compared through spectral analysis. In Section 8, PCA is used to determine the leading patterns of variability in the

atmospheric circulation at 500-hPa. Finally, regression analysis is performed among the various fields to show associated patterns.

4. T_{IR} data

a. PCA of T_{IR} data

Applying PCA to the covariance matrix of monthly T_{IR} anomalies covering the Antarctic continent results in two modes with distinct eigenvalues that meet the separation criteria of North et al. (1982). The leading mode explains 52% of the variance in T_{IR}, while the second mode accounts for 9% of the variance. The first EOF, shown in Fig. 1a as a regression of T_{IR} anomaly data onto the first normalized principal component (T_{IR}-PC1, Fig. 1b) is associated most strongly with the high plateau of East Antarctica. Locally, high correlations in East Antarctica indicate that up to 80% of the variance in T_{IR} can be explained by this first mode, as determined by r^2 values. More moderate correlation of the same sign occurs over West Antarctica. Moderate correlation of opposite sign occurs on the northern reaches of the Antarctic Peninsula.

The second EOF (Fig. 1c) is centered on the Ross Ice Shelf and on the Marie Byrd Land region of the continent. Most of West Antarctica is of the same sign, but the pattern changes sign over the Ronne-Filchner ice shelf (at 60°W) and most of East Antarctica. Some coastal areas near 120°E have the same sign as West Antarctica. Over the central and eastern sections of the Ross Ice Shelf and Marie Byrd Land, high correlation coefficients (not shown) indicate that 40-60% of the T_{IR} variance is explained by mode 2. This is in contrast to the 10-16% of variance in this region explained by mode 1. Only a small fraction of the variance in East Antarctic temperatures can be explained by mode 2. The time-varying component of this structure is given by the normalized principal component (T_{IR}-PC2, Fig. 1d).

b. Seasonality of T_{IR} modes

While the leading patterns of tropospheric circulation variability, including the SAM, exist year-round in the SH middle and high latitudes (Cai and Watterson 2002; Gong and Wang 1999; Thompson and Wallace, 2000), the range of Antarctic temperature variability is much larger in winter months than summer months (King and Turner 1997; Shuman and Stearns, 2001). In T_{IR}, the standard deviation of July monthly means is about twice that of January monthly means, averaged over the continent. In winter, longwave radiation terms dominate the surface energy budget and strong surface inversions develop during clear and calm weather. Therefore, the surface temperature in winter is very sensitive to factors that disturb the inversion, particularly changes in cloudiness and winds (van den Broeke 2000b; Warren 1996). Since PCA modes are designed to maximize variance explained, the leading T_{IR} modes may be more characteristic of winter than of summer temperature variability.

PCA is performed on seasonal subsets of the data: Summer (DJF), Autumn (MAM), Winter (JJA), and Spring (SON). The short time series diminish the statistical significance of the modes compared to the full data set; however, the following results can be supported. Mode 1 in every season dominates explained variance compared to the subsequent modes (Table 1), but explains slightly more variance in the transition seasons than the solstitial seasons. Compared to the full data set, the mode 1 EOF pattern is most similar in spring and summer, rather than the winter, as might be expected due to the larger variance in winter months. In spring and summer, a large part of the variance is explained over a broad region of East Antarctica, and most of the continent has the same sign. In autumn and winter, EOF 1 has considerably less coherent large-scale spatial structure (i.e. the patterns appear to be more random). However, for all seasons, the correlation of the leading PC and the seasonal SAM index is about 0.5 – 0.6, as shown in Table

properties, while the T_{IR} data vary on much larger length scales, reflecting more closely the surface temperature.

6. Emissivity variability at microwave wavelengths

The emissivity parameterization helps to quantify the effects of the physical properties of the snow layer from which the T_B signal emanates. T_B is the physical temperature of the snow times its emissivity (ε), integrated over the penetration depth (Zwally 1977; Surdyk 2002). This is the Rayleigh-Jeans approximation, allowing a calculation of 37 GHz ε through the relation $\varepsilon = T_B \times T_{IR}^{-1}$. On annual mean or longer timescales, using T_{IR} data in place of the physical temperature of the snow is valid, as mean emissivity changes little and the mean annual surface temperature approximates the mean physical temperature of the snow (Zwally 1977, Surdyk 2002). Co-registration of T_{IR} and T_B data enables a map of ε to be calculated based on the 1982-1999 means (Fig. 2a). The pattern shows a spatial variation in ε of 0.25. This includes the melt areas, which have not been excluded from the T_B data in this section of our study. Although the average spatial variations in ε were removed from the analysis of SS02 by the use of anomalies and the masking of melt zones, the influences of spatially varying ε do affect the appearance of EOF-regression maps in some areas, especially near the margins of the ice sheet. Melting can temporarily make the magnitude of T_B anomalies greater than that of T_{IR} anomalies due to the high absorption of the liquid water.

$$T_B = \varepsilon\, T_{IR}$$

Temporally, ε is negatively correlated with the annual cycles of T_{IR} and T_B when averaged over the continent, and the apparent magnitude of the seasonal change in ε is about 0.02 (Fig. 2b). However, this magnitude is partly artifact, as the T_B annual amplitude (19 K) is 30% less than the T_{IR} annual amplitude (27 K). This ~30% attenuation is indicative of an average penetration depth of less than 1 m (Surdyk 2002). Thus, the true seasonal variation in ε must be

$$\delta\, T_{B\varepsilon} =$$

less than the apparent magnitude obtained when the attenuation is ignored (Surdyk 2002). An

attenuation map can be produced by dividing the average magnitude of the T_B annual cycle by

the magnitude of the T_{IR} annual cycle (not shown). By inference, the more damped the annual

cycle, the deeper the penetration depth (Surdyk 2002). The spatial pattern in attenuation is

highly correlated with the emissivity map, showing that low emissivity corresponds to shallow

penetration depth and vice versa, consistent with the theory that grain size is the dominant factor

affecting both parameters (Surdyk 2002). Annual mean time series of T_{IR} and T_B are positively

correlated, while the calculated emissivity is anti-correlated with T_B and T_{IR} (Fig. 2c). The

calculated interannual range in the value of ε is on the order of 0.01 with a standard deviation of

0.0034. This calculated value of 0.01 is likely close to the real range in ε over the penetration

depth because the annual mean surface temperature (from T_{IR}) approximates the annual mean

temperature at depth. Thus, given the mean annual T_{IR} value of 239 K and the mean ε of 0.86,

the interannual standard deviation in ε accounts for only ~0.8 K of (microwave brightness)

temperature difference, well within the uncertainties of both data sets (Shuman and Comiso

2002) and well below the magnitude of temperature anomalies that are explained by our modes

in Section 7.

7. Maximum Covariance Analysis of the data sets

Maximum Covariance Analysis (MCA) optimizes the covariance explained by pairs of

structures in two data sets. Bretherton et al. (1992) and Wallace et al. (1992) provide a detailed

discussion of the methodology, which is adhered to below. The name singular value

decomposition (SVD) is often applied to the entire method; here it is only used in reference to

the algorithm used in extracting empirical structures via cross-covariance matrix decomposition.

First, the cross-covariance matrix of T_{IR} and T_B anomaly fields is computed (with melting

pixels masked as in SS02). The expansion coefficients of the T_{IR} and T_B fields are found by projecting the singular vectors from SVD onto the original gridpoint data of the respective field. These expansion coefficients are then normalized, and either field can be regressed upon them to display spatial structure. In the case that the T_{IR} (T_B) field is regressed upon a T_{IR} (T_B) expansion coefficient, the map is known as a homogeneous regression map, and in the case that the T_{IR} (T_B) field is regressed upon a T_B (T_{IR}) expansion coefficient, the map is referred to as a heterogeneous regression map.

No formal method has been developed for determining the significance of MCA modes, but some tests apply. The squared covariance fraction (SCF) of each mode is an indication of the fit between the two data sets. Another indication is the correlation coefficient between each mode's pair of expansion coefficients. Additionally, the cross-covariance matrix can be tested for relatedness (before applying MCA) with root mean squared covariance (RMSC, square root of the squared covariance (SC) after dividing by the product of the variance of the two data sets). The high T_{IR}-T_B RMSC of 0.22 implies strongly coupled fields that are suitable for MCA, as RMSC of 0.1 or greater is a typical guideline for strong correlation (Wallace et al. 1992).

MCA applied to T_{IR} and T_B fields yields three significant modes, with a SCF of 77%, 11%, and 5%, respectively. The modes' three pairs of expansion coefficients ($T_{IR}x1$ and T_Bx1; $T_{IR}x2$ and T_Bx2; $T_{IR}x3$ and T_Bx3) are correlated at 0.70, 0.61, and 0.78, respectively (Table 2). In both T_{IR} and T_B, the set of homogeneous regression maps for the leading two modes are almost identical to the leading spatial patterns from PCA of the data sets considered separately. These maps (not shown) are essentially the same as Fig. 1a and 1c for the T_{IR} field and SS02 Fig. 2a and 2c for the T_B field, a further indication that the two data sets are well correlated.

The set of heterogeneous regression maps, displayed in Fig. 3, are similar to cross-regressions and show the anomaly in the field on the map associated with one standard deviation of the opposite field's expansion coefficient. For mode 1, the T_{IR} field regressed onto T_Bx1 (Fig. 3a) is similar to the first EOF of T_{IR} anomalies, although less variance in T_{IR} is explained (23%). The T_B field regressed onto $T_{IR}x1$ (Fig. 3b) produces a pattern that is more smoothly varying than the first EOF of T_B (see SS02, Fig. 2a), and explains 11% of the variance. The amplitudes in Fig. 3b are smaller than those in Fig. 3a, implying attenuation of the surface temperature signal through the penetration depth. Also, where the covariance in Fig. 3b is the greatest in East Antarctica, notably between 75°S and 80°S, the emissivity is lowest, as shown in Fig. 2a, consistent with shallow microwave penetration depths and little attenuation. In Fig. 3c, the T_{IR} field is regressed onto T_Bx2, explaining 3% of the variance in T_{IR}, and the resulting pattern is similar to the second EOF of T_{IR}. Likewise, regression of the T_B field onto $T_{IR}x2$ (Fig. 3d), explains 4% of the variance, and produces a heterogeneous map similar to the second EOF of T_B. In this pair of maps, the amplitudes are comparable in magnitude, consistent with little attenuation, a shallow penetration depth, and low emissivity in the Ross Sea sector of Antarctica (Fig. 2a).

A third mode is diagnosed with MCA that was not prominent in the PCA results for the data sets when considered separately (although this third MCA mode correlates well with the fourth mode in T_{IR} data alone and the fifth mode in T_B data alone). It is retained for discussion because it projects onto the linear trends in the T_{IR} and T_B data sets and is reproducible, as discussed below. Because the $T_{IR}x3$ and T_Bx3 expansion coefficient time series have upward trends (see Fig. 4c, below), these time series and the T_{IR} and T_B gridpoint data are both detrended prior to the construction of the heterogeneous regression maps in order to avoid spurious

correlations. If the trends are retained in the time series, the heterogeneous maps of mode 3 look very similar to annual mean trends in the T_{IR} and T_B data sets (see Kwok and Comiso 2002, Fig. 2, for trends in T_{IR}). Therefore, care must be taken not to include spurious correlations of unrelated trends in the maps. The map with T_{IR} data regressed onto T_Bx3 explains 4% of T_{IR} variance and shows positive anomalies in T_{IR} throughout much of East Antarctica (Fig. 3e). The anomalies of greatest magnitude occur from 0° to 60°E. Similarly, the map of T_B data regressed onto $T_{IR}x3$, explains 4% of T_B variance and shows positive T_B anomalies, but of weaker magnitude, in the same area of East Antarctica.

The results outlined above strongly imply that there is meaningful covariance between T_{IR} and T_B data sets (Table 3). However, it must be established with confidence that the correlations have not arisen by chance. As a first test of reproducibility, T_{IR} and T_B anomaly data are detrended prior to MCA. In this case, the same three modes are produced, but without the trend in the third mode. Second, as a test of the statistical robustness of the MCA results, the T_{IR} and T_B data sets are divided into subsets. Data for odd months only are used, and then, data for even months only. Odd and even month RMSC, SC, SCF, and correlation coefficients between expansion coefficient pairs are comparable in magnitude to the statistics for the full data sets for each of the first three modes (Table 3), indicating that the first three modes meet reproducibility criteria.

Another test of statistical robustness, based on the following Monte Carlo procedure, further demonstrates the strong relationships between T_{IR} and T_B anomaly data. Following the method of Wallace et al. (1992), the temporal order of the T_{IR} field is scrambled randomly while the order of the T_B field remains unchanged. RMSC, SC, SCF and correlation coefficients are computed for each of 1000 random runs (Table 3). The significance of the observed runs and the

15

subsets clearly stands out above the random runs. The observed squared covariance is an order of magnitude larger than the mean SC of the scrambled runs, the SCF of the observed first mode is about two standard deviations above the mean of the scrambled runs, and the correlation coefficients among expansion coefficient pairs for the first three modes are well above the mean of the scrambled runs. Finally, the RMSC values of the random data sets are smaller than the value of 0.1 that would indicate strong correlation. This leaves little doubt as to the significance, above the 99% confidence level, of the leading MCA modes and the strong relationship between the T_{IR} and T_B fields.

The three pairs of normalized expansion coefficients show the time variability of the three surface temperature modes from MCA (Fig. 4). The expansion coefficients of the first two modes are well correlated with the original PCs from each data set considered separately, as can be seen in Table 2. For instance, T_{IR}-PC2 correlates with T_{IR}x2 at $r = 0.96$ and similarly high correlations exist for the other matches. Therefore, the time series that explain the most covariance between the T_{IR} and T_B data sets also explain the most variance in the individual data sets.

Because T_B time series correspond to temperature signals over some depth of the snow and firn, it is expected that they should be damped compared to the surface temperature, as determined by the period of the temperature forcing and the depth of the microwave emission (see Fig. 10 of Surdyk 2002). The MCA procedure is unable to completely remove this effect, but it does show that the T_B and T_{IR} have a common forcing—the surface temperature. The strong covariance also suggests that effects of the clear sky bias in T_{IR} data and snow emissivity influences on T_B data do not mask the underlying leading modes of surface temperature variability.

The power spectra of each expansion coefficient time series are estimated with a Hanning window providing 13 degrees of freedom (Fig. 5). Also shown in Fig. 5 is the theoretical spectrum, with 95% confidence limits, for the first order red noise autoregressive process (AR(1)) that provides the best fit to each time series (von Storch and Zweirs 1999). There are no significant spectral peaks at the 99% confidence level. Each time series is consistent with red noise, but with different degrees of "redness," which can be quantified by comparing the AR(1) coefficients from the best-fit theoretical spectrum.

If it is assumed *a priori* that T_{IR} spectra provide a direct measure of the variability in the surface temperature, then T_B spectra should reflect the attenuation of that variability at depth. Because both the penetration depth and the surface forcing are spatially variable, the degree of attenuation will also be spatially variable, and this is reflected in differences among the pairs of AR(1) coefficients. For Mode 1 (Fig. 5a), the distributions of spectral power in both T_{IR} and T_B are nearly identical, consistent with a shallow microwave penetration depth and low emissivity in the region of greatest covariance in Mode 1. In Modes 2 and 3, the T_B spectra (Fig. 5b, 5c) show significant enhancement at low frequencies compared with the T_{IR} spectra. That is, the T_B time series are "redder" and have greater AR(1) coefficients than do the T_{IR} time series. In Mode 3, this is consistent with the relatively high emissivity (see Fig. 2a) and deep penetration depth in the East Antarctic region associated with Mode 3. For Mode 2, the "redness" of the T_Bx2 spectrum is enhanced by the relatively flat spectrum of the surface forcing. As suggested by the T_{IR} spectra and expansion coefficient time series for Mode 2, high frequency, month-to-month variability dominates the overall variability in the area of the ice sheet (West Antarctica) that contributes most of the variance to Mode 2. Note that while the region where Mode 2 is most dominant (Siple Coast area of West Antarctica) is actually characterized by relatively low

emissivity, high emissivity and deep penetration depth is found elsewhere in West Antarctica, especially along the coasts of the Amundsen and Bellinghausen Seas. These spectral analysis results are thus generally consistent with the physical relationship expected between the two types of data.

8. Influence of atmospheric circulation on Antarctic temperatures

a. Principal Component Analysis of 500-hPa geopotential height anomalies

To define the leading patterns of SH atmospheric circulation during the time period of this study, PCA is applied to monthly Z500 anomaly data poleward of 20°S. For equal-area weighting, the data are weighted by the square root of the cosine of their latitude prior to analysis. The original unweighted Z500 data are regressed against each normalized PC, showing anomalies corresponding to one standard deviation of the corresponding PC. Three patterns of interest are resolved, explaining 24%, 12%, and 10% of the (weighted) variance respectively. The latter two patterns are not well separated under the criteria of North et al. (1982). However, they have been reported by a number of studies and found in many different data sets (Carleton 2003; Cai and Watterson 2002; Mo and White 1985). Our results are consistent with the definition of the first Z500 pattern as the SAM (Fig. 6a), the second Z500 pattern as the Pacific South American (PSA) pattern (Fig.6b), and the third pattern as the zonal wavenumber-3 pattern (Fig. 6c) as named by other studies (Cai and Watterson 2002 and references therein). The signs are displayed for consistency with the modes in T_{IR} and T_B and the regression patterns discussed below.

b. Correlations and regression patterns

Associations between Antarctic temperatures and patterns of atmospheric circulation can be illustrated with a variety of methods. The temporal correlations among the PCs of Z500, the

expansion coefficient pairs from MCA, and the Southern Oscillation Index (SOI) are summarized in Table 4. The first PC of Z500 forms a representative SAM index (Thompson and Solomon 2002), and it has strong correlation with the first MCA mode (r(T_{IR} x1, SAM) = 0.58 and r(T_Bx1, SAM) = 0.61) and weak correlation with the other modes. Z500 PC2 correlates well with the SOI (r = 0.43), and has moderate correlation with both modes 1 and 2 in T_{IR} and T_B. Z500 PC3 has a weak correlation with the SOI (r = 0.18) and the best correlation with mode 2 in T_{IR} and T_B (r(T_{IR} x2, Z500 PC2) = 0.39 and r(T_Bx2, Z500 PC2) = 0.32). Mode 3 from MCA has only weak correlation with the Z500 patterns, as r(T_{IR} x3, SAM) = 0.15 is the strongest value.

Regression patterns reinforce the connections implied by the various correlation coefficients. Since T_{IR} and T_B data are highly correlated, regressions involving Z500 data discussed here are made only with T_{IR} data for illustration. Regressions of T_{IR} data onto the normalized PCs of the three leading Z500 patterns are shown in Fig. 7. The SAM explains 17% of the variance in T_{IR} anomalies (Fig. 7a), the PSA pattern explains 6% of the variance (Fig. 7b), and the zonal wavenumber-3 pattern explains 3% of the variance (Fig. 7c). The first regression pattern is quite similar to the first T_{IR} EOF (Fig. 1a). During the positive phase of the SAM, relatively strong westerlies encircle Antarctica near 60°S, which tends to enhance warm air advection over the northern Peninsula, while the cool anomalies on the rest of the continent are indicative of adiabatic cooling (Thompson and Wallace 2000).

As seen in Fig. 7b, in East Antarctica, the PSA pattern explains much less variance in surface temperature than does the SAM, but the spatial structures of temperature anomalies are generally similar. In the Peninsula and most of West Antarctica, the PSA pattern explains variability of the same sign as in East Antarctica. However, the PSA pattern is associated with

19

temperature anomalies of opposite sign near 150°W, 75°S, consistent with the anticyclonic 500-hPa height anomaly centered near 60°S, 125°W (Fig. 6b).

The PSA regression pattern resembles the regression of T_{IR} data upon the SOI that was shown in Fig. 3b of Kwok and Comiso (2002). For comparison to the PSA pattern in geopotential height, we show the pattern in Z500 associated with the Southern Oscillation, formed by regressing Z500 data onto the negative SOI to illustrate anomalies typical of El Niño years (Fig. 8). The zonally elongate north-south dipole structure over the far southern Pacific closely resembles the ENSO warm minus cold year mean 500-hPa height difference of Renwick and Revell (1999 Fig. 5) and the ENSO-associated patterns of other studies (e.g. Mo and Higgins 1998, Kidson 1999; Bromwich et al. 2003). In contrast to the 6% of T_{IR} variance explained by the PSA pattern, our calculations indicate that only 0.5% of the variance in T_{IR} anomalies on the Antarctic continent is explained by the regression of T_{IR} data upon the SOI. However, circulation indices such as the SOI may not adequately capture the variability that is truly associated with ENSO (Carleton 2003; Kidson and Renwick 2002). ENSO-related forcing in the tropics is thought to project primarily onto the PSA pattern of variability on interannual to interdecadal timescales in middle to high latitude SH geopotential height field (Cai and Watterson 2002, Garreaud and Battisti 1999).

It is interesting that the pattern in Antarctic T_{IR} explained by the PSA pattern also resembles the regression (although of opposite sign) of winter temperatures at Faraday station upon the T_{IR} gridpoint data (King and Comiso 2003, Fig. 1). Although King and Comiso (2003) suggested that the climate variability of the Antarctic Peninsula is unrelated to the rest of Antarctica, our results show a connection through the PSA pattern. As illustrated in Fig. 6b, the strong anticyclonic anomaly in the far southeastern Pacific is accompanied by low geopotential

height over most of Antarctica. Thus there is a connection between the anomalous meridional advection along the western Peninsula implied by the southeastern Pacific center of action and contemporaneous decreases in geopotential height over most of the continent.

As shown in Fig. 7c., the wavenumber-3 pattern explains positive temperature anomalies over the same area of West Antarctica associated with the second surface temperature mode, consistent with the strong positive and negative height anomalies centered along 60°S near 90°W and 155°W, respectively. The wavenumber-3 pattern also explains weak temperature anomalies of the same sign in East Antarctica, unlike the second temperature mode, in which West and East Antarctica are out of phase. This is likely due to the additional influence of the PSA pattern on the second surface temperature mode. While the PSA pattern in Z500 is associated with geopotential height fluctuations over East Antarctica, the wavenumber-3 pattern has very little correlation with heights over this region.

As a consistency check, Z500 data are now regressed upon T_{IR} expansion coefficients from the leading MCA modes. As above, the time series of mode 3 are detrended prior to regression. Although T_{IR} expansion coefficients are used here for illustration, regressions involving T_B expansion coefficients are very similar. The first Z500 regression pattern (Fig. 9a) closely resembles the SAM pattern in Z500 (Fig. 6a), especially in the Eastern Hemisphere. In the west, the PSA (Fig. 6b) pattern appears to have an influence on both the first and second regression patterns (Fig. 9a and 9b). However, the second regression pattern (Fig. 9b) most strongly correlates with the Z500 wavenumber-3 pattern (Fig. 6c). The third regression pattern (Fig. 9c) resembles the SAM, but has anomalies of much weaker magnitude. The positive anomalies in East Antarctica near 45°E are suggestive of a ridge in the mid-troposphere extending inland through East Antarctica. Hirasawa et al. (2000) and Enomoto et al. (1998)

show that this condition is a blocking high that pumps warm, moist air from the north all the way to the polar plateau. The positive temperature anomalies associated with the third mode (Fig. 3e) correspond to the "strip" of annual mean warming on the East Antarctic ridge observed by Kwok and Comiso (2002). Inspection of monthly trends shows that in winter months, warming trends in T_{IR} occur over a much broader area than this strip, and Comiso (2000) described several anomalously warm July episodes in East Antarctica. Since the winter months account for most of the trend in the mode 3 expansion coefficients, it is likely that the events explained by mode 3 and these warm episodes are part of the same phenomenon.

9. Discussion and Conclusions

Previous studies have shown that Antarctic 37 GHz T_B data and T_{IR} data are both well correlated with surface air temperatures (Shuman and Comiso 2002; Surdyk 2002; Shuman and Stearns 2001; Comiso 2000), but this is the first to fully examine the consistency of these relationships across the continent. The PCA and MCA results demonstrate that the most important empirical modes in the T_{IR} and T_B data sets are well correlated with each other. The strength of the connection between T_{IR} and T_B increases confidence in the quality of both data sets. A general difference between the data sets is that the T_B data are more spatially varying and more temporally autocorrelated than the T_{IR} data because of the dependence of T_B on both emissivity and temperature integrated over a layer of snow and firn. The most prominent differences between corresponding time series of T_{IR} and T_B modes are attributable to attenuation of surface temperature signals through the snow. The degree of dampening depends on the period of the forcing and the penetration depth of the microwave emission. Lower emissivity regions indicate a shallow penetration depth and relatively high-amplitude T_B fluctuations, which results in the highest T_{IR} and T_B covariance. The calculated spatial pattern in

emissivity apparently changes very little in time, and most likely represents spatially differing snow and firn structures.

Spatial and temporal patterns of T_{IR} and T_B variability, and more generally, surface temperature variability, in Antarctica are consistent with well-documented patterns of variability in extratropical SH atmospheric circulation. It is clear that the most important influence on Antarctic temperature anomalies from month-to-month to interannual timescales is the SAM. The SAM is well separated from other modes in both Z500 data and the satellite data sets. Looking at data from all months, strong temperature trends associated with this mode are not seen. However, inspection of trends by month over the length of the record shows that T_{IR} observations are consistent with a late spring and summer cooling trend, possibly driven by an increasing tendency of the SAM to stay in its positive phase during these seasons (Thompson and Solomon 2002).

The PSA pattern has an influence on the first two surface temperature modes. The wavenumber-3 pattern of variability, however, has a relatively stronger influence on the second surface temperature mode, shown by its association with large temperature anomalies in the West Antarctic sector inland of the Ross and Amundsen seas. Anomalies of opposite sign in East Antarctica imply that the PSA pattern exerts a stronger influence there. Since ENSO-related variability projects primarily onto the PSA and the wavenumber-3 patterns, Antarctic climate records show ENSO-like spectra (SS02; Ichiyanagi et al. 2002; Bromwich and Rogers 2001; White et al. 1999).

Some persistent trends in the available satellite record are associated with the third mode, which cannot, within the scope of this study, be clearly linked to the principal patterns of atmospheric circulation variability. However, blocking events over inland East Antarctica have

been documented with station data (Hirasawa et al. 2000; Enomoto et al. 1998) and provide a plausible explanation for the trends in temperature and the pattern seen in Z500 on our regression map (Fig. 9c). During these episodes, rises of ~40 K can occur in two days or less at remote interior stations such as Dome Fuji and Plateau, and T_a can take more than a month to return to its value before the rise (Enomoto et al. 1998; Kuhn et al. 1973). The upward trend in the T_{IR} and T_B expansion coefficients comes primarily from the winter months, when the blocking episodes most often occur and the surface temperature is extremely sensitive to circulation changes. In addition, changes in cloud cover and winds associated with blocking will destroy the surface inversion, adding to the magnitude of the surface temperature anomalies (Hirasawa et al. 2000). At present, however, the satellite record is too short to establish the long-term significance of the trends, and the monthly temporal resolution of this study limits our ability to further characterize the causes of variability in the third temperature mode.

The results of this study show that the surface temperature variability of Antarctica is well represented by both the T_{IR} and T_B data sets. Nonetheless, it is important to note that biases in the T_{IR} data associated with cloud cover, and in the T_B data associated with attenuation and possible emissivity changes, have not been completely removed. Ongoing improvements to the data include a technique for filling in cloud gaps in infrared observations with emissivity-corrected T_B observations (Shuman, personal communication 2002) and a method suggested by Winebrenner et al. (submitted to *Ann. Glaciol.*, 2003) that models T_B data on the basis of T_a variations and which could lead to an improved parameterization of snow properties and their influence on T_B. Analyses of updated data sets may result in minor changes to the empirical modes we have calculated.

Currently, a gap exists between our understanding of Antarctica's short instrumental and satellite records, and deep ice cores from Antarctica (e.g. Petit et al., 1999; Morgan et al. 2002). Future work will include testing the stability of the temperature and circulation modes discussed here on longer timescales. Some prior work suggests that our results will apply. For instance, long ice core paleoclimate records from locations spread thousands of kilometers apart in East Antarctica are well correlated with each other, consistent with our first mode, while records from West Antarctica and some East Antarctic cores appear to reflect local climate, consistent with our second mode (Watanabe et al. 2003; Steig et al. 2000). East Antarctic isotopic records from the ice cores may be tied to the SAM over a large area (Noone and Simmonds 2003), while West Antarctic ice core records would be expected to be strongly linked to circulation variability in the Southern Pacific, which in turn is teleconnected to the tropical Pacific during strong El Niño and La Niña events (Bromwich et al. 2003). Century-scale reconstructions of the major modes of SH atmospheric circulation from tree rings (Jones and Widmann 2003) and a network of intermediate-depth Antarctic ice cores (Mayewski 2003) will help to fill in the gap between our understanding of modern climate variability and our theories of past climate variations.

Acknowledgements

Library at Columbia University (http://iridl.ldeo.columbia.edu). Gerard Roe provided code for autoregression modeling.

REFERENCES

Bretherton, C.S., C. Smith, and J.M. Wallace, 1992: An Intercomparison of Methods for Finding Coupled Patterns in Climate Data, *J. Climate*, **5**, 541-560.

Bromwich, D. H. and A. N. Rogers, 2001: The El Niño-Southern Oscillation modulation of West Antarctic precipitation. *Ant. Res. Ser.*, **77**, 91-104.

Bromwich, D.H., A.J. Monaghan, and Z. Guo, 2003: Modeling the ENSO modulation of Antarctic climate in the late 1990s with Polar MM5, *J. Climate*, in press.

Cai, W., and I.G. Watterson, 2002: Modes of interannual variability of the southern hemisphere circulation simulated by the CSIRO climate model. *J. Climate*, **15**, 1159-1174.

Carleton, A.M., 2003: Atmospheric teleconnections involving the Southern Ocean, J. Geophys. Res., **108**(C4), 8080, doi: 10.1029/2000JC000379.

Comiso, J. C., 2000: Variability and trends in Antarctic surface temperatures from in situ and satellite infrared measurements, *J. Climate*, **13**, 1674-1696.

Doran, P.T., and Coauthors, 2002: Antarctic climate cooling and terrestrial ecosystem response, *Nature*, **415**, 517-520.

Enomoto, H., H. Motoyama, T. Shiraiwa, T. Saito, T. Kameda, T. Furukawa, S. Takahashi, Y. Kameda, and O. Watanabe, 1998: Winter warming over Dome Fuji, East Antarctica, and the semiannual oscillation in the atmospheric circulation, *J. Geophys. Res.*, **103**, D18, 23,103-23,111.

Garreaud, R. D., and D.S. Battisti, 1999: Interannual (ENSO) and interdecadal (ENSO-like) variability in the Southern Hemisphere tropospheric circulation, *J. Climate*, **12**, 2113-2123.

Gillett, N.P., and D.W.J. Thompson, 2003: Simulation of recent Southern Hemisphere climate change, *J. Climate*, submitted.

Gloersen, P., D. Cavalieri, W. J Campbell, and J. Zwally, 1990: Nimbus-7 SMMR polar radiances and Arctic and Antarctic sea-ice concentrations on CD-ROM, National Snow and Ice Data Center, Boulder, CO.

Gong, D., and S. Wang, 1999: Definition of Antarctic Oscillation Index, *Geophys. Res. Lett.*, **26** (4), 459-462.

Hines, K.M., D.H. Bromwich, and G.J. Marshall, 2000: Artificial surface pressure trends in the NCEP-NCAR Reanalysis over the Southern Ocean and Antarctica, *J. Climate*, **13**, 3940-3952.

Hirasawa, N., H. Nakamura, and T. Yamanouchi, 2000: Abrupt changes in meteorological conditions observed at an inland Antarctic station in association with wintertime blocking, *Geophys. Res. Lett.*, **27** (13), 1911-1914.

Ichiyanagi, K., Numaguti, A., and K. Kata, 2002: Interannual variation in stable isotopes in Antarctic precipitation in response to El Niño -Southern Oscillation, *Geophys. Res. Lett.*, **29**(1), 10.129/2000GL012815.

Jones, J., and M. Widmann, 2003: Instrument and tree ring based estimates of the Antarctic Oscillation, *J. Climate*, in press.

Kalnay, E., and Coauthors, 1996: The NCEP/NCAR 40-Year Reanalysis Project, *Bull. Amer. Metero. Soc.*, **77**, 437-472.

Kidson, J.W., 1988: Interannual variations in the Southern Hemisphere circulation, *J. Climate*, **1**, 1177-1198.

Kidson, J.W., 1999: Principal modes of Southern Hemisphere low-frequency variability obtained from NCEP-NCAR Reanalysis, *J. Climate*, **12**, 2808-2830.

Kidson, J.W., and J.A. Renwick, 2002: The Southern Hemisphere evolution of ENSO during 1981-1999, *J. Climate*, **15**, 847-863.

King, J.C., 1994: Recent climate variability in the vicinity of the Antarctic Peninsula, *Int. J. Climatol.*, **14**, 357-369.

King, J.C., and J. Turner, 1997: *Antarctic Meteorology and Climatology*. Cambridge University Press, 409 pp.

King, J.C., and J.C. Comiso, 2003: The spatial coherence of interannual temperature variations in the Antarctic Peninsula, *Geophys Res. Lett*, 30(2), 10.129/2002GL015580.

Kistler, R., and Coauthors, 2001: The NCEP-NCAR 50-Year Reanalysis: Monthly means CD-ROMS and Documentation, *Bull. Amer. Metero. Soc.*, **82**, 247-268.

Kuhn, M.H., A.J. Riordan, and I.A., Wagner, 1973: The Climate of Plateau Station, in *Climate of the Arctic*, Geophysical Institute, University of Alaska, pp. 255-267.

Kwok, R., and J.C. Comiso, 2002: Spatial patterns of variability in Antarctic surface temperature: Connections to the Southern Hemisphere Annular Mode and the Southern Oscillation, *Geophys. Res. Lett.*, **29**(14), 10.1029/2002GL015415.

Maslanik, J. and J. Stroeve, 1990-2001: DMSP SSM/I daily polar gridded brightness temperatures on CD-ROM, National Snow and Ice Data Center, Boulder, CO.

Marshall, G.J., 2002a: Analysis of recent circulation and thermal advection change in the northern Antarctic Peninsula, *Int. J. Climatol.*, **22**, 1557-1567.

Marshall, G.J., 2002b: Trends in Antarctic geopotential height and temperature: A comparison between NCEP-NCAR and radiosonde data, *J. Climate.*, **15**, 659-674.

Mayewski, P.A., 2003: Antarctic Oversnow Traverse-based Southern Hemisphere Climate Reconstruction *EOS, Transactions, American Geophysical Union*, **84**(12), 205..

Mo, K.C., and G.H. White, 1985: Teleconnections in the Southern Hemisphere, *Mon. Wea. Rev.*, **113**, 22-37.

Mo, K.C., and R.W. Higgins, 1998: The Pacific South American modes and tropical convection during the Southern Hemisphere winter, *Mon. Weather. Rev.*, **126**, 1581-1596.

Morgan, V., M. Delmotte, T. van Ommen, J. Jouzel, J. Chappellaz, S. Woon, V. Masson-Delmotte, and D. Raynaud, 2002: Relative timing of delglacial and climate events in Antarctica and Greenland, *Science*, **297**, 1862-1864.

Noone, D., and I. Simmonds, 2002: Annular variation in moisture transport mechanisms and the abundance of 18O in Antarctic Snow, J. Geophys. Res., 107(D24), 4742, 10.129/2002JD00262.

North, G. R., T. L. Bell and R. F. Cahalan, 1982: Sampling errors in the estimation of empirical orthogonal functions, *Mon. Weather Rev.*, **110**, 699-706.

Petit, J.R., and Coauthors, 1999: Climate and atmospheric history of the past 420,000 years from the Vostok ice core, Antarctica, *Nature*, **399**, 429-436.

Renwick, J.A., and M.J. Revell, Blocking over the south Pacific and Rossby wave propagation, *Mon. Weather Rev.*, 127, 2233-2247.

Ribera, P., and M.E. Mann, 2003: ENSO-related variability in the Southern Hemisphere, 1948-2000, *Geophys Res. Lett.*, **30(1)**, 10.129/2002GL015818.

Schneider, D.P., and E.J. Steig, 2002: Spatial and temporal variability of Antarctic ice sheet microwave brightness temperatures, *Geophys. Res. Lett.*, 29(20), doi:10.129/2002GL15490.

Shuman, C.A., and Stearns, C.R., 2001: Decadal length composite inland West Antarctic temperature records, *J. Climate*, **14**, 1977-1988.

Shuman, C.A. and J.C. Comiso, 2002: In situ and satellite surface temperature records in Antarctica, *Ann. Glaciol.*, **13**, 113-120.

Steig, E.J., Morse, D.L., Waddington, E.D., Stuiver, M., Grootes, P.M., Mayewski, P.A., Whitlow, S.L. and M.S. Twickler, 2000: Wisconsinan and Holocene climate history from an ice core at Taylor Dome, western Ross Embayment, Antarctica. *Geograf. Annal.* **82A**, 213-235.

Surdyk, S., 2002: Using microwave brightness temperature to detect short-term surface air temperature changes in Antarctica: An analytical approach, *Remote Sens. Environ.* **80**, 256-271.

Thompson, D. W. J. and J. M. Wallace, 2000: Annular Modes in the extratropical circulation. Part I: Month-to-month variability, *J. Climate*, **13**, 1000-1016.

Thompson, D.W.J., and S. Solomon, 2002: Interpretation of recent southern hemisphere climate change, *Science*, **296**, 895-899.

van den Broeke, M., 2000a: On the interpretation of Antarctic temperature trends, *J. Climate*, **13**, 3885-3889.

van den Broeke, M., 2000b: The semiannual oscillation and Antarctic climate, part 5: Impact on the annual temperature cycle as derived from the NCEP/NCAR reanalysis, *Climate Dyn.*, **16**, 369-377.

Vaughan, D.G., G.J. Marshall, W.M. Connolley, J.C. King, and R. Mulvaney, 2001: Devil in the detail, *Science*, 293, 1777-1779.

von Storch, H., and F.W. Zweirs, 1999: Statistical Analysis in Climate Research. Cambridge University Press, 484 pp.

Wallace, J.M., Smith, C., and C.S. Bretherton, 1992: Singular Value Decomposition of Wintertime Sea Surface Temperature and 500-mb Height Anomalies, *J. Climate*, **5**, 561-576.

Warren, S.G., 1996: Antarctica, in *Encyclopedia of Climate and Weather*, Oxford University Press, 32-39.

Watanabe, O., J. Jouzel, S. Johnsen, F. Parrenin, H. Shoji, and N. Yoshida, 2003: Homogeneous climate variability across East Antarctica over the past few glacial cycles, *Nature*, **422**, 509-512.

White, J. W. C., E.J. Steig, J. Cole, E.R. Cook and S.J. Johnsen, 1999: Recent, annually resolved climate as recorded in stable isotope ratios in ice cores from Greenland and Antarctica. *Amer. Met. Soc. Sym. Glob. Clim. Change Stud.*: **10**, 300-302.

Zwally, H.J., 1977: Microwave emissivity and the accumulation rate of polar firn, *J. Glaciol.*, **18**, 195-215.

Zwally, H. J. and S. Fiegles, 1994: Extent and duration of Antarctic surface melting, *J. Glaciol.*, **40** (136), 463-476.

Table Headings

TABLE 1. Variance explained by first two

PCA modes of T_{IR} and correlation with the

SAM index by season.

TABLE 2. Correlation coefficients among PCs of T_B and T_{IR} considered separately and

expansion coefficients from MCA. Sign is ignored.

TABLE 3. Summary of MCA reproducibility tests and Monte Carlo results.

TABLE 4. Summary of correlation coefficients among modes in Z500 and MCA expansion

coefficients. Sign is ignored.

Figure Captions

Fig. 1. Results from PCA of monthly 1982-1999 T_{IR} anomaly data. (a) EOF-1 shown as a regression coefficient between each grid point and the first normalized PC. (b) The first normalized PC corresponding to the EOF pattern above. (c) As in a but for the second EOF. (d) As in b but for the second PC. Color scale is in K, corresponding to a typical anomaly associated with each mode, that is, the value of one positive standard deviation of the respective PC.

Fig. 2. (a) Mean microwave emissivity at 37 GHz vertical polarization of the Antarctic ice sheet based on 1982-1999 mean values of T_{IR} and T_B. (b) Continent-averaged annual cycles of emissivity, T_B, and T_{IR} based on 18-yr means of each month. (c) Continent-averaged interannual variations of emissivity, T_B, and T_{IR}.

Fig. 3. Heterogeneous regression maps from MCA of T_{IR} and T_B fields. The top panels (a,c,e) are covariances from the T_{IR} field regressed upon the first, second, and third normalized T_B expansion coefficients, respectively. The bottom panels (b,d,f) are covariances from the T_B field regressed upon the first, second, and third normalized T_{IR} expansion coefficients, respectively. Color is in units of K, corresponding to one standard deviation of the respective expansion coefficient.

Fig. 4. Expansion coefficients of the first three MCA modes (a-c, respectively) corresponding to the heterogeneous maps in Fig. 3.

Fig. 5. Power spectra (heavy solid lines) of the MCA expansion coefficients shown in Fig. 4. for (a) first, (b) second, and (c) third modes. Also shown (thin solid lines) are the theoretical spectra of the AR(1) (red noise) process that best fits the original time series. 5% and 95% confidence levels are indicated by dashed lines; 99% confidence level by dotted lines. The coefficients a_1 of the best-fit spectra are also indicated inside the plots.

Fig. 6. The leading modes in monthly 500-hPa geopotential height, 1982-1999. The (a) first, (b) second, and (c) third EOFs, shown as the Z500 data regressed upon the leading normalized PCs. Percentage of variance explained indicated at lower left. Contour interval 5m, zero contour heavy solid line, negative contours dotted, positive contours solid.

Fig. 7. Regressions of T_{IR} gridpoint data upon the first three Z500 normalized PCs (a-c, respectively). Percentage of variance explained indicated in lower left. Color scale is in K, corresponding to one standard deviation of the respective PC time series.

Fig. 8. Regression of 1982-1999 monthly Z500 data upon the SOI with sign reversed to show anomalies typical of the ENSO warm phase. Units, contours as in Fig. 6.

Fig. 9. Regression of Z500 data upon the (a) first, (b) second, and (c) third normalized T_{IR} expansion coefficients shown in Fig. 4. Units, contours as in Fig. 6.

TABLE 1. Variance explained by first two

PCA modes of T_{IR} and correlation with the

SAM index by season.

Season	Mode 1	Mode 2	r(SAM index*,T_{IR}-PC1)
DJF	49%	14%	0.63
MAM	50%	9%	0.49
JJA	49%	13%	0.68
SON	57%	7%	0.50
Full Year	52%	9%	0.57

* The SAM index is the first principal component of 500-hPa geopotential height as discussed in

the text.

TABLE 2. Correlation coefficients among PCs of T_B and T_{IR} considered separately and expansion coefficients from MCA. Sign is ignored.

	T_B-PC1	T_{IR}-PC1	T_B-PC2	T_{IR}-PC2	T_Bx1	T_{IR}x1	T_Bx2	T_{IR}x2	T_Bx3	T_{IR}x3
T_B-PC1	1	.46	0	.11	.81	.47	.21	.05	.01	.04
T_{IR}-PC1		1	.05	0	.68	.99	.01	.11	.00	.02
T_B-PC2			1	.48	.03	.04	.96	.56	.14	.02
T_{IR}-PC2				1	.09	.02	.54	.96	.13	.36
T_Bx1					1	.70	.07	.00	.07	.00
T_{IR}x1						1	.00	.09	.00	.00
T_Bx2							1	.61	.11	.00
T_{IR}x2								1	.00	.15
T_Bx3									1	.78
T_{IR}x3										1

TABLE 3. Summary of MCA reproducibility tests and Monte Carlo results.

Run	SC	RMSC	SCF(%) modes(1,2,3)	$r(T_Bx,T_{IR}x)$ modes(1,2,3)
1000 Scrambled Runs				
Highest	6.3×10^4	.098	(82,31,18)	(.34,.39,.38)
Lowest	1.6×10^4	.050	(29,04,03)	(.14,.16,.16)
Mean	3.1×10^4	.068	(55,14,09)	(.23,.28,.28)
Std. Dev.	7.2×10^3	.008	(10,04,02)	(.03,.04,.04)
Observations				
	3.28×10^5	.223	(77,11,05)	(.70,.61,.78)
Odd Months Only				
	3.27×10^5	.241	(77,11,05)	(.74,.54,.80)
Even Months Only				
	3.32×10^5	.222	(70,16,06)	(.69,.67,.75)

TABLE 4. Summary of correlation coefficients among modes in Z500, SOI, and MCA expansion coefficients. Sign is ignored.

	SOI	$T_B x1$	$T_{IR} x1$	$T_B x2$	$T_{IR} x2$	$T_B x3$	$T_{IR} x3$
Z500-PC1	.16	.61	.58	.06	.05	.06	.15
Z500-PC2	.43	.25	.31	.24	.17	.06	.06
Z500-PC3	.18	.09	.16	.32	.39	.02	.00
SOI		.02	.04	.19	.14	.06	.11

Fig. 1. Results from PCA of monthly 1982-1999 T_{IR} anomaly data. (a) EOF-1 shown as a regression coefficient between each grid point and the first normalized PC. (b) The first normalized PC corresponding to the EOF pattern above. (c) As in a but for the second EOF. (d) As in b but for the second PC. Color scale is in K, corresponding to a typical anomaly associated with each mode, that is, the value of one positive standard deviation of the respective PC.

Fig. 2. (a) Mean microwave emissivity at 37 GHz vertical polarization of the Antarctic ice sheet based on 1982-1999 mean values of T_{IR} and T_B. (b) Continent-averaged annual cycles of emissivity, T_B, and T_{IR} based on 18-yr means of each month. (c) Continent-averaged interannual variations of emissivity, T_B, and T_{IR}.

Fig. 3. Heterogeneous regression maps from MCA of T_{IR} and T_B fields. The top panels (a,c,e) are covariances from the T_{IR} field regressed upon the first, second, and third normalized T_B expansion coefficients, respectively. The bottom panels (b,d,f) are covariances from the T_B field regressed upon the first, second, and third normalized T_{IR} expansion coefficients, respectively. Color is in units of K, corresponding to one standard deviation of the respective expansion coefficient.

Fig. 4. Expansion coefficients of the first three MCA modes (a-c, respectively) corresponding to the heterogeneous maps in Fig. 3.

Fig. 5. Power spectra (heavy solid lines) of the MCA expansion coefficients shown in Fig. 4. for (a) first, (b) second, and (c) third modes. Also shown (thin solid lines) are the theoretical spectra of the AR(1) (red noise) process that best fits the original time series. 5% and 95% confidence levels are indicated by dashed lines; 99% confidence level by dotted lines. The coefficients a_1 of the best-fit spectra are also indicated inside the plots.

Fig. 6. The leading modes in monthly 500-hPa geopotential height, 1982-1999. The (a) first, (b) second, and (c) third EOFs, shown as the Z500 data regressed upon the leading normalized PCs. Percentage of variance explained indicated at lower left. Contour interval 5m, zero contour heavy solid line, negative contours dotted, positive contours solid.
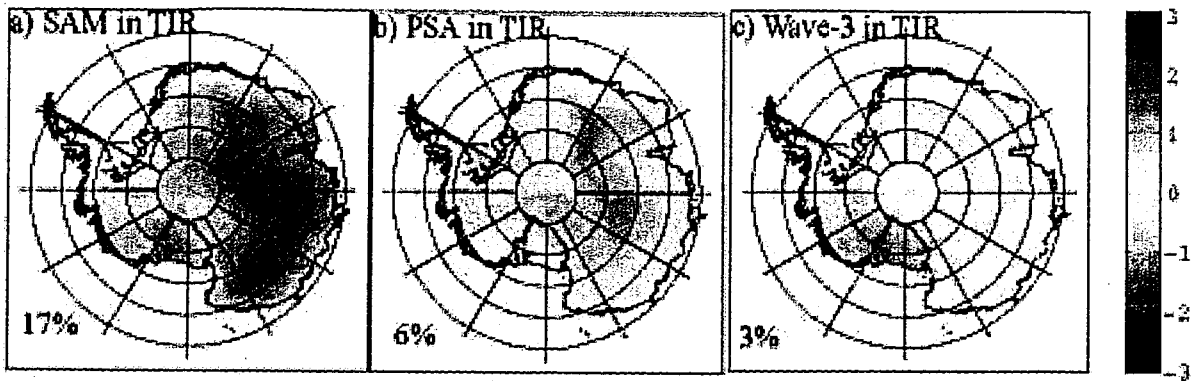
Fig. 7. Regressions of T_{IR} gridpoint data upon the first three Z500 normalized PCs (a-c, respectively). Percentage of variance explained indicated in lower left. Color scale is in K, corresponding to one standard deviation of the respective PC time series.
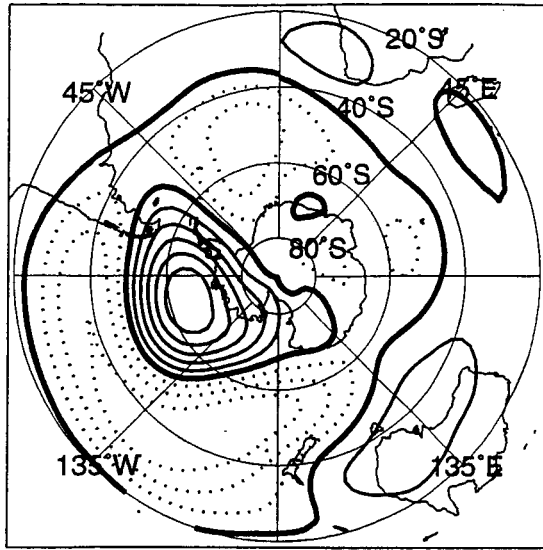
43

Fig. 8. Regression of 1982-1999 monthly Z500 data upon the SOI with sign reversed to show anomalies typical of the ENSO warm phase. Units, contours as in Fig. 6.
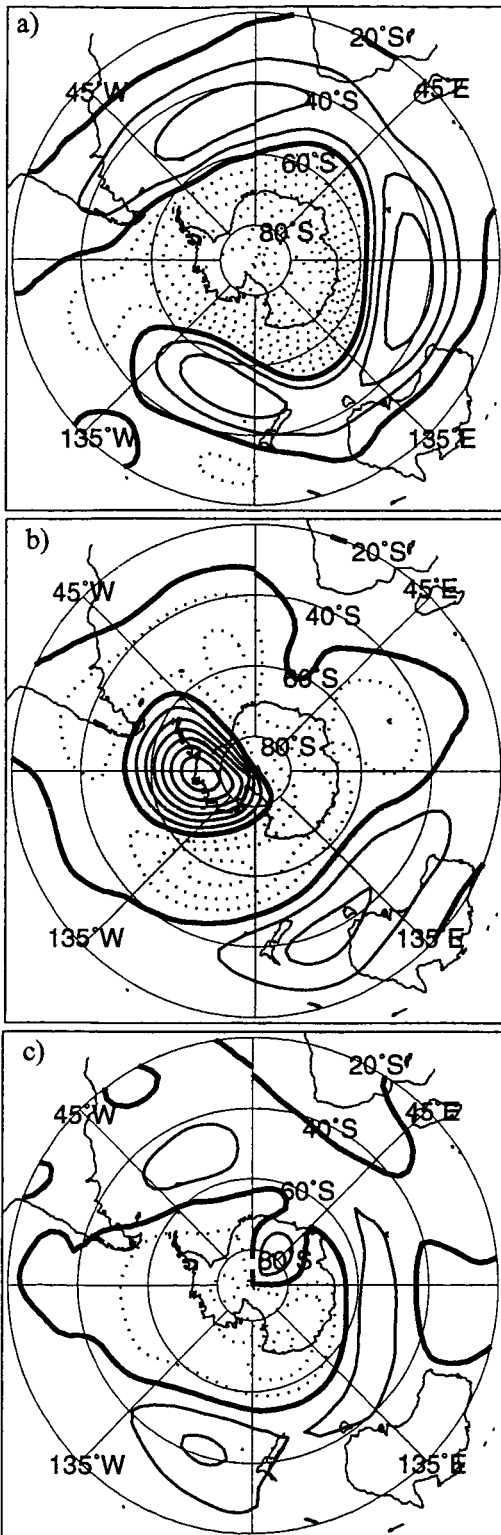
Fig. 9. Regression of Z500 data upon the (a) first, (b) second, and (c) third normalized T_{IR} expansion coefficients shown in Fig. 4. Units, contours as in Fig. 6.